



Ultracold neutron storage in a bottle coated with the fluoropolymer CYTOP

Thomas Neulinger^{1,2,a}, Douglas Beck², Euan Connolly^{1,3}, Skyler Degenkolb^{1,4}, Peter Fierlinger⁵, Hanno Filter^{1,5}, Jürgen Hingerl^{1,5}, Pontus Nordin¹, Thomas Saerbeck¹, Oliver Zimmer¹

¹ Institut Laue-Langevin, Grenoble 38042, France

² University of Illinois Urbana-Champaign, Urbana, IL 61801, USA

³ University of Bristol, Bristol BS8 1TL, UK

⁴ Universität Heidelberg, Heidelberg 69120, Germany

⁵ Technische Universität München, Garching 80805, Germany

Received: 14 March 2022 / Accepted: 11 July 2022

© The Author(s) 2022

Communicated by Alexandre Obertelli

Abstract The fluoropolymer CYTOP was investigated in order to evaluate its suitability as a coating material for ultracold neutron (UCN) storage vessels. Using neutron reflectometry on CYTOP-coated silicon wafers, its neutron optical potential was measured to be 115.2(2) neV. UCN storage measurements were carried out in a 3.81 CYTOP-coated aluminum bottle, in which the storage time constant was found to increase from 311(9) s at room temperature to 564(7) s slightly above 10 K. By combining experimental storage data with simulations of the UCN source, the neutron loss factor of CYTOP is estimated to decrease from $1.1(1) \times 10^{-4}$ to $2.7(2) \times 10^{-5}$ at these temperatures, respectively. These results are of particular importance to the next-generation superthermal UCN source SuperSUN, currently under construction at the Institut Laue-Langevin, for which CYTOP is a possible top-surface coating in the UCN production volume.

1 Introduction

Over the past several decades, experiments with stored ultracold neutrons (UCN) have produced increasingly precise measurements of fundamental properties of the neutron [1–10]. Consequently, comparisons of these results to theoretical predictions have emerged as powerful tests of candidate theories beyond the Standard Model of particle physics. In many such measurements, continued improvements to exper-

imental sensitivity will rely on increased statistics from next generation high-density UCN sources.

The continued development of “superthermal” UCN sources offers one promising route to realizing such gains, as the UCN densities possible in a superthermal source at a given temperature are greater than those obtainable by moderation of neutrons to the same temperature [11]. In such sources, incident neutrons transfer a large fraction of their kinetic energy to the low-energy excitations of a refrigerated converter medium via inelastic scattering, becoming “ultracold” [11–13]. In many experimental realizations, this converter medium is housed in a production volume that is essentially a UCN trap, having walls that reflect UCN but that are transparent to the incident beam of higher-energy neutrons. UCN produced in this manner may be delivered to an experiment by opening a mechanical valve and allowing them to escape from the source through a system of guides. Some projects currently under development, notably the neutron electric dipole moment experiment at the Spallation Neutron Source [14], propose to produce UCN and carry out the measurement of interest within the same volume.

The SuperSUN source, currently under construction at the Institut Laue-Langevin (ILL) in Grenoble, France, is planned to supply UCN to the PanEDM neutron electric dipole moment experiment [15]. Its design [16] makes use of superfluid ^4He as the superthermal converter medium, and builds on earlier successful prototypes [17–22]. Significant gains in UCN density were achieved in prototypes by manually applying a thin layer of Fomblin grease, a fluorinated lubricant with approximate monomer formula $\text{C}_3\text{F}_6\text{O}$ [23], over the beryllium-coated walls of the production volume. However, these coatings have been observed to slowly flow

^a e-mail: neulinger@ill.fr (corresponding author)

over time, thinning in some regions and clumping up in others, thus motivating the investigation of new, stable coating materials.

The fluoropolymer CYTOP was identified as a potential alternative for the SuperSUN production volume for several reasons. For one, having similar elemental composition to Fomblin, CYTOP, with approximate monomer formula $C_6F_{10}O$, should possess comparable neutron absorption characteristics. In addition, CYTOP is a physically durable and chemically resistant coating material developed for industrial use, whose thickness may be precisely controlled via manufacturer specified coating processes. Like Fomblin, CYTOP coatings are also hydrophobic. This chemical property is important to reduce surface concentrations of hydrogen, a species that is frequently associated with large UCN losses [23–25]. All these features are especially desirable for the preparation of low loss, stable, uniform coatings on storage surfaces that are subject to mechanically and thermally harsh cryogenic environments, as will be present in the SuperSUN production volume.

This work reports on measurements of the UCN storage properties of CYTOP coatings. A brief theoretical survey of UCN storage in material traps is presented in Sect. 2. The experimental determination, by neutron reflectometry, of the neutron optical potential of CYTOP is the subject of Sect. 3. The characteristic storage times of a bottle whose inner surface is coated with CYTOP, between room temperature and approximately 10 K, are discussed in Sect. 4. Estimates of the neutron loss factor η , using the measured neutron optical potential of CYTOP and neutron storage data, are given in Sect. 5.

2 Theoretical background

For sufficiently low neutron energies, all materials possess an effective neutron “optical” potential [26], typically on the order of 10^{-7} eV, which is

$$V = \frac{2\pi\hbar^2}{m_n} \sum_i \rho_i a_i, \quad (1)$$

where m_n is the neutron mass, and ρ_i and a_i are the number density and bound coherent scattering length, respectively, of the nuclear species i . When a free neutron of kinetic energy E encounters a thick wall of potential $V > E$, it will be reflected for any angle of incidence. In this context, “thick” means several multiples of the penetration depth, $\delta_p = \hbar [8m_n(V - E)]^{-1/2} \sim 0.1 \mu\text{m} (V - E)^{-1/2}$ for V and E in units of neV. (See Appendix A.) Therefore, bottles whose inner surfaces present such potentials may trap—or store—neutrons, which are then said to be “ultracold”.

The time scale on which UCN may be stored in bottles is greatly influenced by absorption and inelastic scattering of the storage material. Their effect on UCN storage may be described analytically by means of a complex potential $U = V - iW$, in which

$$W = \frac{\hbar}{2} \sum_i \rho_i \sigma_i v', \quad (2)$$

where the σ_i are the total loss cross sections (absorption + inelastic) of the nuclear species i , and v' is the neutron velocity in the material [27]. In the UCN regime, nuclear resonances are absent, and $\sigma_i \propto 1/v'$ [28], so that the product $\sigma_i v'$ is independent of the neutron energy. The loss probability per wall interaction, or per “bounce”, μ , is then equal to the product of a constant “loss factor” $\eta \equiv W/V$, and a function of order unity $f = f(E/V)$. (See Appendix A.)

In some cases, a simple but realistic treatment of neutron storage assumes a uniform spatial density and an isotropic velocity distribution of UCN in a bottle of volume \mathcal{V} and surface area A . In this case, the loss rate per UCN r as a function of energy E is

$$r(E) = \frac{1}{\tau_\beta} + \bar{\mu}(E) \frac{Av}{4\mathcal{V}}, \quad (3)$$

where the free neutron lifetime is $\tau_\beta = 879.4(6)$ s according to the Particle Data Group [29], $\bar{\mu}(E)$ —Eq. A3—is the angle-averaged loss probability per wall interaction, and $Av/4\mathcal{V}$ is the rate of wall collisions, with $v = \sqrt{2E/m_n}$ the UCN velocity. ($v \sim 0.5 \text{ m s}^{-1} \sqrt{E}$ for E in neV.) In this expression, all additional sources of loss—for example, that due to the presence of residual gases [30,31] in the bottle—have been neglected.

The total number of UCN in the storage bottle N_b after storage for time t_s is

$$N_b(t_s) = \int dE n_b(E) \exp(-r(E)t_s), \quad (4)$$

where $n_b(E)$ is the energy distribution of UCN present in the bottle at $t_s = 0$. Experimentally, it is sometimes found—as in the present work—that measurements of N_b are reasonably well described by a decaying exponential function

$$f(t_s) = N_0 \exp(-t_s/\tau_s), \quad (5)$$

in which case τ_s is referred to as the storage time constant of the bottle. (t_s is the independent variable, whereas N_0 and τ_s are fit parameters.) Typically, inelastic scattering cross sections depend on temperature T , so that $\eta = \eta(T)$, and variation of τ_s with temperature is frequently observed. See, for example, Ref. [32], which discusses additional sources of variation of τ_s with temperature.

3 Reflectometry measurements

In order to determine the neutron optical potential of CYTOP, time-of-flight cold neutron reflectometry was performed on two thin film samples [33] at the ILL in Grenoble, France on instrument D17 [34]. A pulsed beam with a wavelength band of $\lambda = 2$ to 28 Å and known intensity spectrum impinges at a shallow angle of $\theta \sim 1^\circ$ on a thin film sample, and the reflectivity is measured as the ratio of the intensity of the reflected to the incident beam, as a function of neutron “wave-vector transfer” perpendicular to the sample surface: $Q = \frac{4\pi}{\lambda} \sin \theta$. (See Appendix A). Fits of theoretical models of the sample reflectivity to these data enable the extraction of, among other parameters, the optical potential of the surface CYTOP layer. Samples 1 and 2 were prepared on polished silicon wafers dip-coated [35] in CTL-107MK product [36] using pull speeds of 0.5 mm s $^{-1}$ and 1 mm s $^{-1}$, respectively. The samples were subsequently dried in air for 15 min, and then baked at 130 °C for 45 min to harden and achieve polymer cross-linking.

Raw reflectivity data were corrected for background and instrument effects using the LAMP/COSMOS software [37]. These refined data are plotted in Fig. 1 as a function of the wave-vector transfer Q . Vertical error bars represent statistical uncertainties, while horizontal error bars are the full-width half maxima (FWHM) of Gaussian approximations to the “resolution functions” appropriate for a given configuration of the D17 instrument. A resolution function $f_Q(Q')$ describes the range of physically different Q' values that contribute to the reflectivity at a nominal value of the momentum transfer Q on a real instrument. When its width is small compared to the features of the reflectivity curve, $f_Q(Q')$ may be approximated by a Gaussian having the same variance as the actual $f_Q(Q')$ [38].

The refined data were used to fit a function $\tilde{R}(Q)$ that, at a given value of momentum transfer Q , is the convolution of an ideal reflectivity model $R_{\text{model}}(Q)$ and the resolution function $f_Q(Q')$. That is

$$\begin{aligned} \tilde{R}(Q) &= \int dQ' f_Q(Q') R_{\text{model}}(Q') \\ &= \int dQ' \frac{\exp\left(-\frac{(Q'-Q)^2}{2\sigma^2(Q)}\right)}{\sqrt{2\pi\sigma^2(Q)}} R_{\text{model}}(Q'). \end{aligned} \quad (6)$$

In the second line, $f_Q(Q')$ is explicitly written as a Gaussian distribution with mean Q and standard deviation $\sigma(Q) = (2\sqrt{2\ln 2})^{-1} \text{FWHM}(Q) \approx 0.4 \text{FWHM}(Q)$. In fitting, several $R_{\text{model}}(Q)$ were analyzed, all of which contained a top layer (CYTOP) of unknown thickness and unknown optical potential— d and V , respectively—and a substrate of infinite

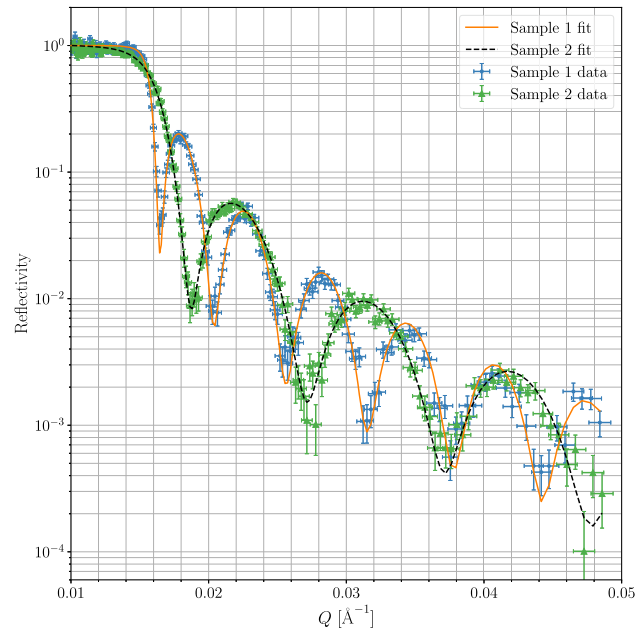


Fig. 1 Neutron reflectivity of two CYTOP thin film samples on silicon substrate. The fits shown in this figure are for the simplest $R_{\text{model}}(Q)$, and give $V = 115.3(1)$ neV, $d = 905.8(4)$ Å, and a reduced chi-squared value of $\chi_r^2 = 1.58$ for Sample 1 (pull speed 0.5 mm s $^{-1}$), and $V = 114.9(1)$ neV, $d = 554.9(4)$ Å, and $\chi_r^2 = 1.03$ for Sample 2 (pull speed 1 mm s $^{-1}$)

thickness and assumed to possess the optical potential of silicon, 53.9 neV, calculated from the scattering length density $\text{SLD} = 2.07 \times 10^{-6}$ Å $^{-2}$ [39], where $\text{SLD} \equiv \sum_i \rho_i a_i$. (See Eq. 1). The simplest of these models contained only these features, while additional models included one or both of two other unknown sample parameters: the thickness and optical potential of a “native oxide” layer on the silicon substrate [40], and an interfacial roughness between layers, defined according to Equation 13 in Ref. [41]. For each model parameter α_i , optimal fit parameters $\hat{\alpha}_i$ were taken to be the least squares estimates, found numerically using the Nelder-Mead algorithm [42]. The parameter covariance matrices were calculated from numerical estimates of $\frac{1}{2} \frac{\partial^2 \chi^2}{\partial \alpha_i \partial \alpha_j}$, where χ^2 is the weighted sum of squares of the residuals to the fit, evaluated at the $\hat{\alpha}_i$. (See, for example, Equation 40.12 in Ref. [29].)

We report the optical potential of CYTOP here as the weighted average across the different fit results of the models, and across the two samples. This was found to be $V = 115.2(2)$ neV, which is in reasonable agreement with $V = 117$ neV predicted by Eq. 1 using tabulated neutron scattering lengths [43] and the density of CYTOP, 2.03 g cm $^{-3}$ [36], and which is slightly higher than the reported value for Fomblin, $V = 106$ neV [44].

4 Storage measurements

4.1 Bottle preparation

The CYTOP storage bottle coating was prepared using an oven system [45–48] originally developed to produce deuterated polyethylene coatings [49,50]. The main body of the bottle assembly is an approximately-cylindrical tube of aluminum of inner diameter and length 90 mm and 589 mm, respectively. A side port and the back end of the main body are capped by aluminum blank flanges, while an aluminum front plate with a 20 mm diameter hole in its center allows UCN to enter (exit) the bottle, and is opened (closed) by a conical, coated stainless steel plug. To coat, the fully-assembled bottle, without the plug, was filled with CTL-107 MK solution and installed in the coating oven with its axis oriented horizontally. It was then rotated about its axis at 6 rpm for the duration of the coating process. To begin, the entire oven was inclined at an angle so that the entrance plate was immersed in solution, and the temperature was brought to 100 °C. After 15 min, the oven was inclined in the opposite sense, to immerse the back plate in solution. 15 min later, the temperature was increased to 150 °C, and the oven was tilted back and forth in intervals of 10 min until no solvent remained. This was monitored by means of a solvent recovery system. Finally, the bottle was baked at 200 °C for 30 min. Based on the quantity of product used and the surface area of the interior of the bottle, it is estimated that the average coating thickness is approximately 15 μm.

The bottle plug was dip-coated in CTL-107MK solution multiple times, using a pull speed of 1 mm s⁻¹. Between dips, the plug was dried between 1 and 5 min in a separate oven at 80 °C, and was finally baked at 200 °C for 30 min. Based on the number of dips and the manufacturer specified dip-coating characteristics of the product, the coating thickness is estimated to be approximately 1.5 μm.

4.2 Apparatus

An overhead diagram of the storage experiment apparatus is shown in Fig. 2. UCN are supplied to the storage bottle through a series of polished stainless steel guides connected to the prototype superthermal source SUN-2 [22], whose UCN production volume is filled with superfluid ⁴He at approximately 0.6 K, and whose inner surface is coated with beryllium followed by a thin layer of Fomblin grease. The source produces UCN by converting a portion of a monochromatic beam of 8.9 Å wavelength “cold” neutrons (CN) into a stored collection of UCN via inelastic single-phonon scattering of neutrons in superfluid ⁴He [11,12]. UCN are extracted vertically from the source through a mechanical UCN valve at the top of the production volume.

In an attempt to qualitatively investigate the dependence of the bottle storage time constant τ_s on the energy spectrum of stored UCN, the SUN-2 source was operated in two modes: “continuous” and “accumulation”. In the former, the CN beam continually illuminates the production volume, and a continuous flow of UCN exits the source through the statically open UCN valve. In the latter, this valve is initially closed, and a higher density of UCN is accumulated in the source until the production rate is balanced by storage losses. When desired, a burst of UCN is delivered to the experiment by opening the UCN valve, meanwhile redirecting the CN beam away from the source. Because the storage loss rate in the production volume, as in any material trap, increases with increasing UCN energy (see $r(E)$ in Eq. 3), the spectrum of UCN in the source becomes biased toward lower energy during accumulation as compared to continuous mode operation, in which UCN spend, on average, a shorter period of time in the production volume.

The first guide section from the source is oriented vertically, and results in a height offset of 360 mm between the horizontal source and bottle axes. Thereafter, all guides leading to the bottle are oriented horizontally, and are of 50 mm inner diameter. 520 mm from the axis of the vertical guide section, a polypropylene ($V \approx -10$ neV calculated from Eq. 1, assuming a density of 0.9 g cm⁻³) vacuum-separation foil (4 μm thick) reinforced by a thin, laser-cut stainless steel mesh with a surface area of 30 mm² separates the source and storage experiment vacuum spaces during measurements. A vacuum gate valve sits 30 mm downstream of this foil and is left permanently open during measurements, but can be closed to independently vent the source or the storage experiment.

The next component in the guide system is a UCN switch, which consists of a 60° stainless steel “elbow” (120° between straight sections) positioned inside a rotating drum whose vertical axis sits 190 mm from the gate valve. The exterior of the drum is coated with an 85/15 nickel-molybdenum alloy, $V > 200$ neV [51], whereas the interior of the switch housing is coated with titanium, $V = -48$ neV [26]. The switch has three positions: in the “filling” position, the switch directs UCN from the source into the horizontal guides leading to the storage bottle; in the “bypass” position, the switch directs UCN from the source toward a UCN detector; and in the “emptying” position, the switch directs UCN exiting the bottle to the detector.

The guides leading to the detector from the UCN switch are first a 90° elbow downward, and then a vertical guide section that widens to 80 mm inner diameter, and which has a 10 mm diameter pumping hole in its side. The detector is a ³He proportional counter [52] with a 50 mm thick, 80 mm diameter cylindrical detection volume filled with 37 mbar of ³He gas, 15 mbar of CO₂ gas, and 1.1 bar of Ar gas. The entrance window to the detector is an aluminum (opti-

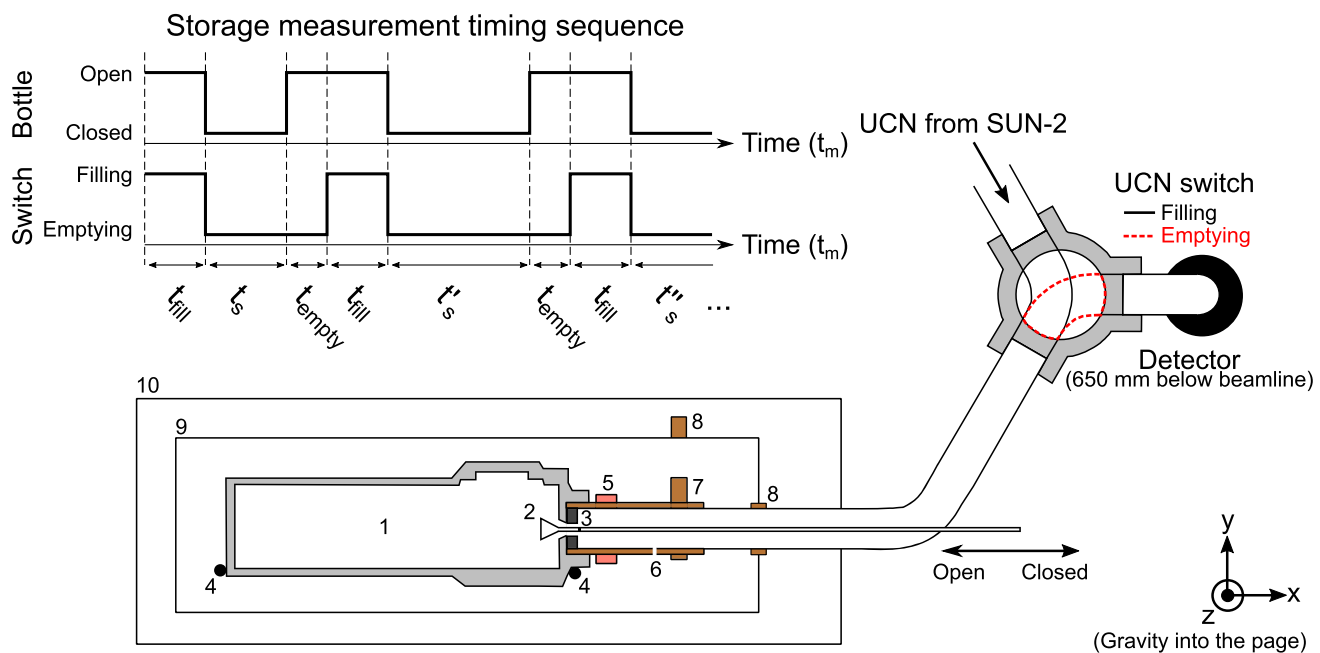


Fig. 2 Top-down view of measurement setup, not to scale. Storage measurement timing sequence at top with varying storage time t_s against measurement time t_m . Gravity points into the page. All elements are shown in the horizontal plane, except for the UCN detector, which sits 650 mm below the axis of the bottle. (1) CYTOP-coated aluminum stor-

age bottle, (2) CYTOP-coated bottle plug, (3) removable stainless steel insert/entrance cover, (4) position of temperature sensors, (5) heater, (6) 3 mm pumping hole, (7) thermal anchoring to second stage of pulse-tube refrigerator (not shown), (8) thermal anchoring to first stage, (9) thermal screen, (10) vacuum vessel

cal potential $V = 54$ neV [26]) foil, approximately 100 μm thick, that lies 650 mm below the bottle axis, far enough to ensure that all UCN falling from the horizontal guides have total velocity sufficient to enter the detection volume. For a neutron, the product $m_{\text{ng}}g \approx 0.1$ neV mm^{-1} , where g is the acceleration due to gravity at the surface of the Earth; thus, a UCN falling 650 mm will gain 65 neV of kinetic energy.

The first guide leading from the UCN switch to the storage bottle is 500 mm in length. It is terminated by a 60° elbow that contains a linear motion vacuum feedthrough used to actuate the storage bottle valve. Thereafter, a 1000 mm-long guide with a copper sleeve brazed to a portion of its exterior runs directly to the storage bottle. This has a 3 mm hole drilled in its side, through both the guide and sleeve, that leads to the primary vacuum space of the storage experiment and enables pumping of the guides and bottle. On the bottle end of this guide, the sleeve has a large, M60×1.5 male thread that mates to the aluminum front plate of the storage bottle assembly, allowing bottles with different coatings or geometries to be installed. 180 mm before the bottle, the sleeve is thermally anchored through a clamp to the second stage of a Sumitomo RP-052A pulse-tube refrigerator, which has a cooling power of 0.5 W at 4.2 K. (See 7 in Fig. 2.) The first stage cools a non-vacuum-tight heat screen enclosing the storage bottle, and is also thermally anchored to the UCN guide further upstream (see 8 and 9 in Fig. 2). This

configuration enables a lowest average bottle temperature of approximately 10 K, with roughly 9 K at the front and 11 K at the back of the bottle. Temperatures are monitored by four sensors: one calibrated Cernox 1050 and one PT-100 on both the front and back of the bottle (see 4 in Fig. 2). A heater wire is clamped around the copper guide sleeve to achieve temperatures between room temperature and the base temperature. Pressures of 2×10^{-6} mbar at room temperature and 7×10^{-7} mbar at the base temperature are typical, as measured in the primary vacuum space, i.e., within 10 in Fig. 2.

The bottle's hole for UCN entrance and exit can be opened (closed) by pushing (pulling) the plug toward (away from) the bottle interior. As with the bottle, this plug can be exchanged, and is installed on the end of a 4 mm diameter steel rod that runs from the vacuum feedthrough down the center of the guide leading to the bottle. (See 2 in Fig. 2.) The uncoated exterior of the front bottle plate is seen by UCN approaching the bottle as an aluminum annulus; some measurements were performed with a stainless steel ($V = 189$ neV [53]) insert covering the exposed aluminum (See 3 in Fig. 2).

4.3 Measurement procedure

A UCN storage measurement consists of three steps: filling, storage, and emptying. (See measurement timing sequence

in Fig. 2). In the first step, the UCN switch is rotated to the filling position with the bottle valve open, allowing UCN from the source to enter the storage bottle for a time t_{fill} . In the second step, the bottle is closed, and the UCN switch is rotated to the emptying position, allowing any UCN stored in the guides between the bottle and the switch to fall into the detector. These guides were observed to be completely emptied within approximately 30 s. In the last step, the bottle is opened after the storage time t_s has elapsed, and UCN are emptied into the detector for a time t_{empty} . A new measurement begins by returning the UCN switch to the filling position. Thereafter, the sequence repeats, using a new value of the storage time t'_s . The values of t_s are drawn from a preselected set in random order without replacement. After exhausting the set, measurements are repeated with the storage times in the same order.

The values for t_{fill} and t_{empty} are different depending on whether the source is operated in continuous or accumulation mode. In the former, for a fixed storage time, the number of UCN detected N was found to be roughly proportional to $1 - \exp(-t_{\text{fill}}/\tau_{\text{fill}})$, where $\tau_{\text{fill}} \approx 50$ s was determined experimentally. A value of $t_{\text{fill}} = 200$ s was therefore deemed sufficient in this mode as a compromise between large N and efficient use of measurement time. In the latter mode of operation, UCN are accumulated in the source for 600 s before filling begins. A filling time of $t_{\text{fill}} = 50$ s was determined experimentally to maximize N . In both modes, the emptying time t_{empty} was chosen to be long enough for the count rate of detected UCN to return to the background level: $t_{\text{empty}} = 120$ s in continuous mode and $t_{\text{empty}} = 140$ s in accumulation mode. The latter value is slightly larger on account of the number of UCN in the bottle being higher in this mode of operation. As discussed in Sect. 4.2, these UCN are expected to have lower average energy.

4.4 Source output and background rate measurements

Measurements of the source output and the background rate were performed immediately prior to and following each series of storage measurements at a given temperature. The source output is the count rate of detected UCN with the source UCN valve open, the UCN switch in the bypass position, and the CN beam incident on the production volume. In continuous mode, the background was measured as the count rate of detected UCN with the UCN switch in the emptying position, the source UCN valve open, and the CN beam incident on the production volume. For accumulation mode, the configuration was the same, except that the CN beam was not incident on the production volume.

Storage measurements took place during two consecutive reactor cycles, 188 and 189, at the ILL, with reactor powers of 56 MW and 43 MW, respectively. During Cycle 188, an average UCN source output rate of approximately

2600 s⁻¹ was observed, varying by less than 3% over an 11 day period of operation, when the storage measurements described below took place. During Cycle 189, a leak in the vacuum-separation foil between the source and the storage experiment resulted in a gradual decrease in the source output rate from roughly 1900 s⁻¹ to 900 s⁻¹ over a 26 day period of operation. It is suspected that the decrease in the source output rate is associated with residual gases, like water vapor, slowly leaking into the source and freezing on the walls of the extraction guides, which are normally filled only with a low pressure of helium gas. This hypothesis is supported by the observation that, when an additional pump was placed on a guide section near the separation foil, the improved vacuum resulted in a change in the rate of decrease of the source output from roughly 6% per day to 3% per day. All storage data presented in this work were taken after the additional pump was installed. Plots of the source output rate over time during Cycles 188 and 189 can be found in Figure 3.5 of Ref. [54].

During Cycle 188, the source was operated only in continuous mode, and a background rate of approximately 0.1 s⁻¹ was observed. During Cycle 189, this background rate was measured to be approximately 0.04 s⁻¹. This decrease resulted from improved shielding of the detector and from a smaller source output rate at lower reactor power; despite the titanium coating on the interior of the switch housing, there is still a small leak of UCN through the switch to the detector. For accumulation mode measurements, a background rate of approximately 0.02 s⁻¹ was observed. Plots of the background rate over time during Cycles 188 and 189 can be found in Figure 3.6 of Ref. [54].

4.5 Results

In order to determine the storage time constants τ_s , the storage measurement data were background subtracted, and decaying exponential fits (Eq. 5) were made to the remaining total number of UCN detected N as a function of storage time t_s . Optimal fit values of N_0 and τ_s are taken to be the least squares estimates, found exactly after taking the natural logarithm of Eq. 5. Uncertainties are estimated by standard error propagation. (See, for example, Section 10.2 in Ref. [55].) Typical data sets from two storage measurements, one at room temperature (red dots) and the other at an average bottle temperature of 10.2 K (blue crosses), are plotted in Fig. 3 on both logarithmic (a) and linear (b) vertical scales. Fits of Eq. 5 to these data give estimates of the storage time constants of $\tau_s = 330(3)$ s and $\tau_s = 585(5)$ s at the two bottle temperatures, respectively. In Fig. 3 the data are shown on two vertical scales because the large spread in the low temperature data is especially apparent on a linear scale. This spread significantly exceeds the error bars on N (estimated as \sqrt{N}), and is much greater than that of the room temperature data.

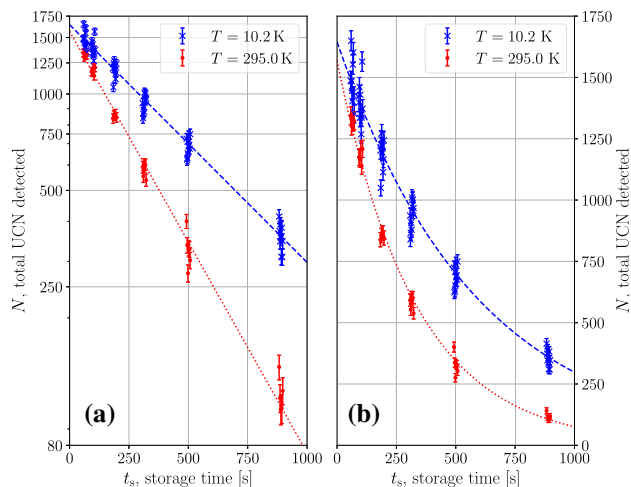


Fig. 3 Typical storage curves for room temperature (red dots) and low temperature (blue crosses) measurements shown on both logarithmic (a) and linear (b) vertical scales. Data are slightly spread horizontally to enable error bars to be seen. Storage times are 65, 100, 190, 315, 500, and 890 s. Note the large vertical spread in the low temperature data. The 295.0 K and 10.2 K data shown here correspond to measurements 10 and 0 in Table 1, respectively

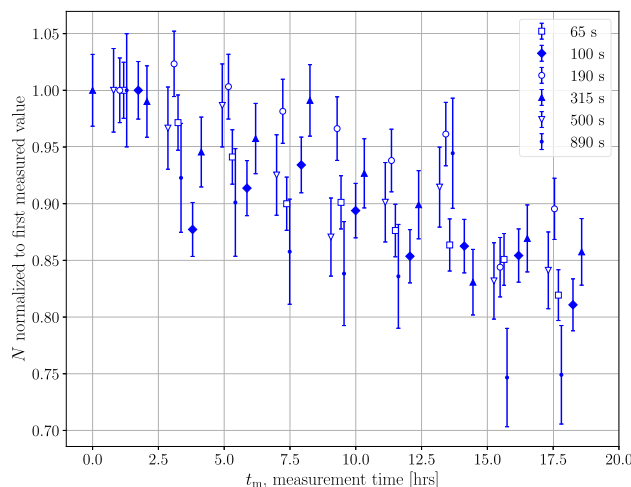


Fig. 4 Gradual decrease in N , the number of detected UCN, shown as a function of measurement time t_m , for the low temperature data of Fig. 3. Data here are grouped by storage time t_s and normalized to the first measured value of N within the group

This large vertical spread appears in many data sets for storage measurements performed below room temperature, and results from a gradual decrease in N over time. Figure 4 visualizes this for the low temperature storage data of Fig. 3 by plotting the N normalized to their first measured values for each storage time against the measurement time t_m , taken to be zero at the beginning of the measurement series. (For a graphical representation of the relationship between t_m and t_s , see the timing diagram in Fig. 2). The normalized N are labeled by their respective values of the storage time t_s . It is suspected that the gradual decrease in N is asso-

ciated with residual gases freezing onto the cold walls of the experiment at low temperatures, resulting in a lossy surface layer. A similar effect was observed at low temperatures in other storage measurements (not reported in this paper) using different coatings, which suggests that the decrease is related to the cryogenic apparatus, and is not specific to the CYTOP coating. Further details of the effect are discussed in Appendix B.

An attempt to correct for the gradual decrease in N was made by fitting to data using an empirically-motivated extension to Eq. 5,

$$f(t_s, t_m) = N_0 \exp(-t_s/\tau_s) \exp(-t_m/\tau_m), \quad (7)$$

in which the additional fit parameter τ_m provides a measure of the time scale of the decrease. Parameter estimates are calculated in the same manner as for Eq. 5. Figure 5 shows an example of the application of Eq. 7 to the low temperature data plotted in Fig. 3, for which there is a large vertical spread. Figure 5a shows these storage data corrected for the gradual decrease in N , that is, divided by the factor $\exp(-t_m/\tau_m)$, which significantly reduces this spread. The gradual decrease may be seen in Fig. 5b, which shows N divided by the factor $N_0 \exp(-t_s/\tau_s)$, that is, the fractional change in counts as a function of measurement time. This plot indicates that a decrease in N of almost 20% occurred over the course of the measurement. Despite this relatively large drop, fits using Eqs. 5 and 7 produce estimates of the storage time constant that are within error bars of one another: $\tau_s = 585(5)$ s and $\tau_s = 583(5)$ s, respectively.

In fact, estimates of τ_s from Eqs. 5 and 7 were found to be within error bars for all storage data, regardless of the temperature at which the measurement was performed. In comparison to the use of Eq. 5, the main effects of fitting with Eq. 7 are to produce larger estimates of N_0 , and to decrease the reduced chi-squared statistic of the fit χ^2_r . The amount by which χ^2_r changes between fits using Eqs. 5 and 7 was used to determine the appropriateness of the latter model in extracting τ_s from a particular set of storage data (See Appendix C). Measurement information and optimal fit parameters for all CYTOP storage data are given in Table 1. The data sets to which Eq. 7 was applied in order to estimate τ_s are those for which τ_m is also given.

Figure 6 shows the estimates of τ_s plotted as a function of the average bottle temperature T . There, it can be seen that the storage time constant increases with decreasing T . In addition, at the temperature extremes, τ_s does not appear to vary greatly between measurements in continuous and accumulation mode, or between measurements with and without the stainless steel insert at the bottle entrance. This suggests that the different measurement configurations produce similar UCN energy spectra in the storage bottle. Near room temperature and slightly above 10 K, the weighted averages

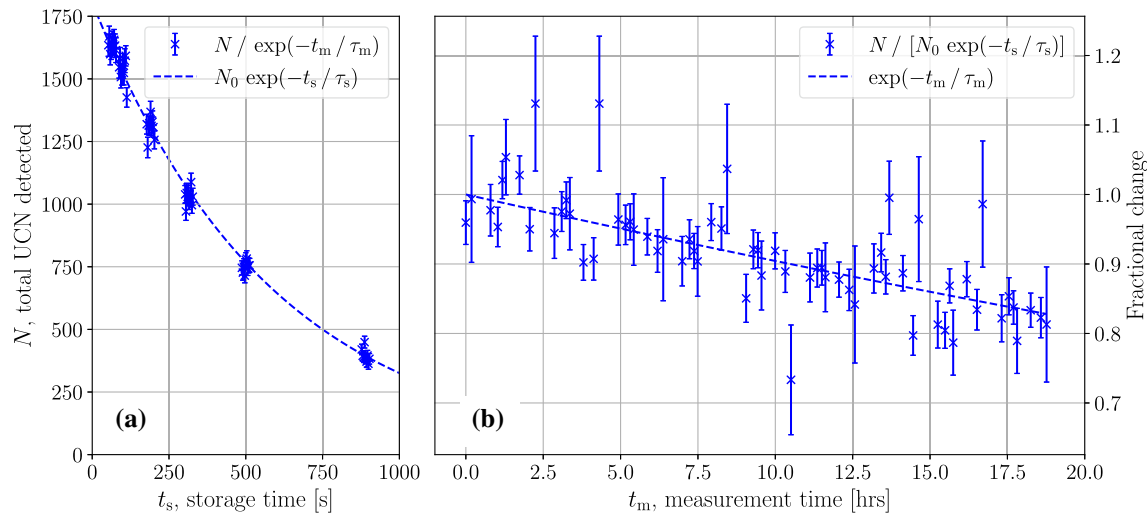


Fig. 5 Example of the application of Eq. 7 to the low temperature data in Fig. 3. **a** Shown on a linear scale, the “corrected” total UCN counts, that is, N divided by the factor $\exp(-t_m/\tau_m)$. Data are slightly spread

horizontally to enable error bars to be seen. **b** The fractional change in the total UCN counts, $N / [N_0 \exp(-t_s/\tau_s)]$

Table 1 Summary table of storage measurement results. Starting from the left, the columns give (Index) a chronological index; (Cycle) the reactor cycle; (Date) the start date and time; (Front) the entrance type to the storage bottle, either the uncovered aluminum, Alu or the stainless steel insert, SS (ν) the size of the data set, i.e., the number of points;

(Mode) the mode of operation of the SUN-2 source, either continuous, “C”, or accumulation, “A”; and (T) the average bottle temperature during the measurement. The next three columns give the least squares estimates of the fit parameters from either Eqs. 5 or 7. The last column gives the reduced chi-squared value of the fit

Index	Cycle	Date [yy/mm/dd]	Front	ν	Mode	T [K]	τ_s [s]	N_0	τ_m [hrs]	χ^2_r
0	188	20/09/17 15h	Alu	65	C	10.2	583(5)	1806(16)	99(7)	1.23
1	188	20/09/18 13h	Alu	15	C	38.9	560(13)	1438(21)	–	1.21
2	188	20/09/18 18h	Alu	15	C	69.1	529(12)	1385(22)	–	0.71
3	188	20/09/19 00h	Alu	49	C	104.8	514(7)	1281(16)	104(20)	1.05
4	188	20/09/19 13h	Alu	15	C	128.3	462(11)	1117(20)	–	0.92
5	188	20/09/19 20h	Alu	15	C	10.5	556(14)	1189(20)	–	1.11
6	188	20/09/20 00h	Alu	35	C	52.8	548(9)	1149(17)	107(38)	0.81
7	188	20/09/20 09h	Alu	15	C	77.0	511(13)	1044(19)	–	1.42
8	188	20/09/21 19h	Alu	16	C	215.2	361(6)	1654(24)	–	1.93
9	188	20/09/22 13h	Alu	15	C	162.8	416(8)	1702(26)	–	1.57
10	188	20/09/22 23h	Alu	38	C	295.0	330(3)	1568(15)	–	2.06
11	189	21/03/12 16h	Alu	26	C	296.3	293(5)	984(15)	–	1.30
12	189	21/03/13 08h	Alu	33	C	13.4	574(11)	1177(11)	–	1.12
13	189	21/03/13 14h	Alu	59	A	11.1	551(5)	2706(20)	126(10)	1.08
14	189	21/03/14 17h	Alu	132	A	280.0	301(2)	2352(17)	315(34)	1.97
15	189	21/03/17 11h	SS	24	C	295.8	303(7)	785(13)	–	1.30
16	189	21/03/17 16h	SS	22	A	295.8	297(4)	1741(21)	–	1.22
17	189	21/03/18 08h	SS	34	C	14.5	577(12)	951(10)	–	0.97
18	189	21/03/18 15h	SS	58	A	11.7	546(6)	2074(18)	149(16)	1.72

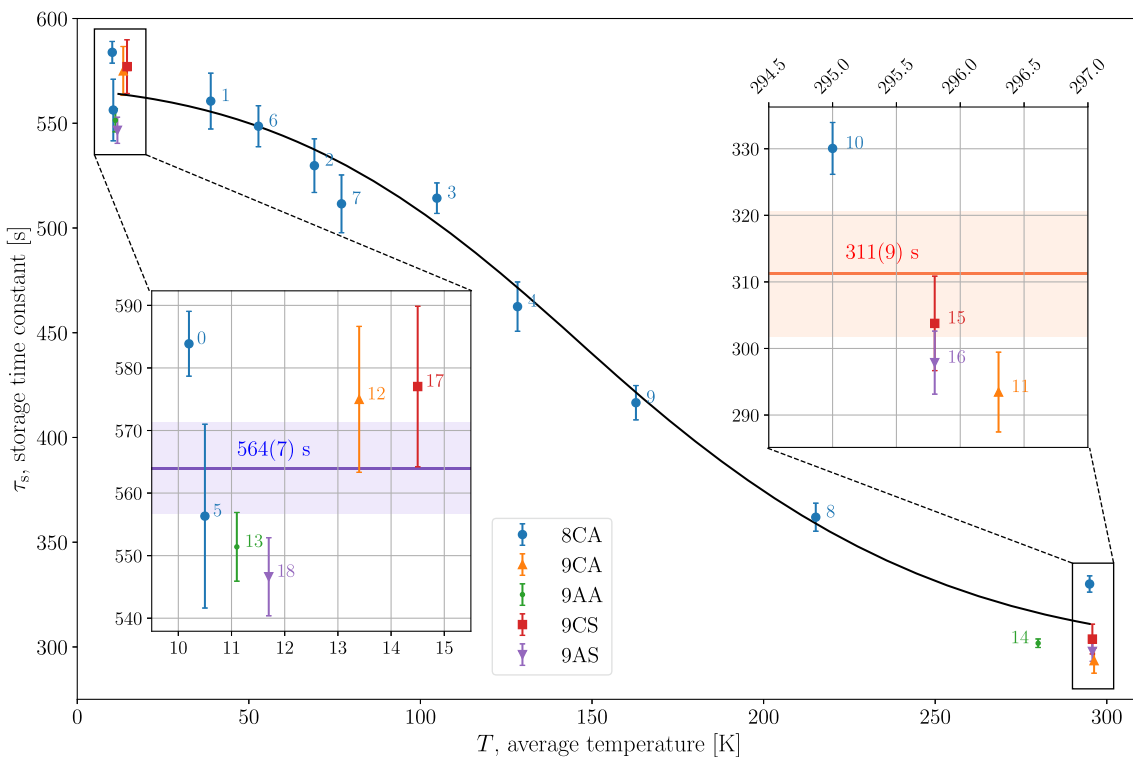


Fig. 6 Estimates of the storage time constants of the CYTOP-coated bottle, τ_s , plotted as a function of the average bottle temperature T . The black line is a guide to the eye. Points are labeled by a chronological index given in Table 1, and are also grouped by a three symbol code XYZ, in which X gives the reactor cycle (“8” for Cycle 188, “9” for 189), Y gives the mode of operation of the source (“A” for accumulation

and “C” for continuous), and Z gives the bottle entrance type (“A” for the bare aluminum and “S” for the stainless steel insert). Left inset: a zoomed-in view of the low temperature τ_s data, for which a weighted average gives 564(7) s, indicated by the blue horizontal line. Right inset: a zoomed-in view of the room temperature τ_s data, for which a weighted average gives 311(9) s, indicated by the red horizontal line

of τ_s are 311(9) s and 564(7) s, respectively. (See the horizontal lines in the insets to Fig. 6). Although the physical mechanism responsible for the temperature variation of the storage time constant has not yet been investigated, values of τ_s within 10% of the low temperature maximum appear to be achievable at 77 K, the boiling point of liquid nitrogen. This property may prove to be convenient in experiments for which the cost or complexity of very low temperature cryogenic equipment is undesirable or prohibitive.

5 Loss factor

In this section, we describe estimates of the loss factor of CYTOP made from experimental storage data. The discussion here is a summary of the detailed treatment given in Ref. [54]. N_b , the number of UCN in the storage bottle at time t_s , is modeled by Eq. 4, that is, as an integral over the product of the initial energy distribution of UCN in the bottle when it is closed, $n_b(E)$, and the factor $\exp(-r(E)t_s)$, which accounts for the loss rate per UCN $r(E)$, and where $r(E)$ depends on η as discussed in Sect. 2. We assume that the number of UCN

detected N is simply proportional to N_b . Thus, we determine the loss factor of CYTOP by fitting N to the function

$$f(t_s) = C \int dE n_b(E) \exp(-r(E)t_s), \quad (8)$$

where C is a fitting parameter and the zero of E is defined with respect to the bottle axis.

There are two main difficulties to this approach. The first is that $n_b(E)$ is not directly measurable. We therefore estimate this distribution by simulation, for which it is necessary to make a number of assumptions about the transmission and storage properties of uncharacterized components in the source, guides, and storage bottle. These assumptions are always made in a way that will tend to produce softer—that is, lower average energy—estimates of $n_b(E)$, which, in turn, results in overestimates of the η of CYTOP. (The loss rate per UCN $r(E)$ increases with increasing energy; thus, a UCN spectrum biased toward higher energy would experience more wall interactions per unit time, and so smaller values of η would better fit a given set of neutron storage data.) The number of assumptions necessary is significantly reduced when the SUN-2 source operates in accumulation

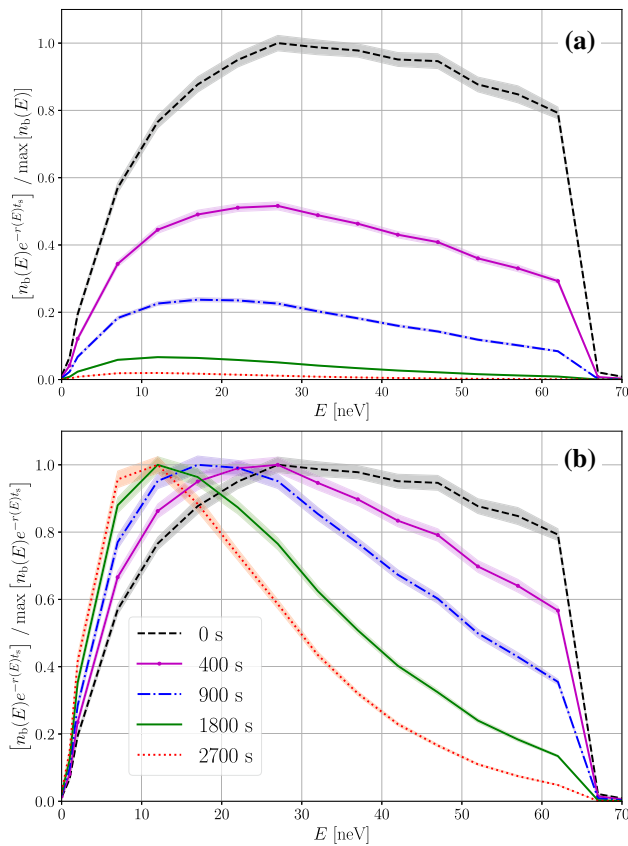


Fig. 7 Example of the time evolution of the integrand of Eq. 8 using the simulated spectrum $n_b(E)$. **a** Shows the integrand normalized to the maximum of $n_b(E)$, while **(b)** shows the integrand normalized to its maximum at each t_s . The legend in **(b)** applies to both plots. Equation 3 is used to model the loss rate per UCN $r(E)$ with the loss factor and optical potential of CYTOP taken to be $\eta = 2.7 \times 10^{-5}$ and $V = 115.2$ neV, respectively. Uncertainty in the spectrum is indicated by the shaded bands, which reflect statistical uncertainty in UCN transport parameters derived from simulation. See Section 4.6 in Ref. [54] for details

mode, as opposed to in continuous mode. For this reason, $n_b(E)$ is only simulated for accumulation mode operation of the source, and only the corresponding measurements are used in estimating the η of CYTOP. (See Appendix E in Ref. [54] for a discussion of several limitations to this approach.) An example of the time evolution of the integrand of Eq. 8 is shown in Fig. 7 using the simulated spectrum $n_b(E)$ and Eq. 3 to model the loss rate per UCN $r(E)$.

The second difficulty in using Eq. 8 to extract the loss factor of CYTOP is that the correct model for the loss rate per UCN $r(E)$ is not known. Equation 3 gives one possibility: the ideal case of an isotropic velocity distribution of UCN, in which gravity is neglected, and the only sources of loss are beta decay and wall interactions. In Appendix D of Ref. [54], $r(E)$ given by Eq. 3 for the present bottle geometry is compared to an analytical expression that accounts for gravitational effects. (Equation 4.17 in Ref. [26].) It is found that, for the energy distribution of UCN calculated by simulation,

gravity may be neglected to good approximation. Concerning additional sources of storage loss, three extensions to Eq. 3 (referred to hereafter as Model 1) were considered: loss due to UCN upscattering and absorption by residual gases in the bottle (Model 2), loss due to gaps in the CYTOP coating that would expose the aluminum of the storage bottle to its interior (Model 3), and loss due to holes in the bottle (Model 4), as might be present, for example, at the interface of the bottle entrance and plug. Model 1 has two fitting parameters: the proportionality constant C and the loss factor of CYTOP η . It treats $n_b(E)$ as an input, as well as the bottle geometry parameters, and the measured value of the optical potential of CYTOP, 115.2(2) neV. Model 2 has an additional parameter X , which is an energy independent quantity representing the UCN loss rate due to the presence of residual gas. Models 3 and 4 each have three parameters: C , η , and a , where a is the surface area of either the gaps or holes respectively. These four models are discussed in detail in Section 5.1 of Ref. [54].

There are four storage measurements in which the SUN-2 source was operated in accumulation mode, and which may therefore be analyzed according to the approach described above: measurements 13, 14, 16, and 18. (See Table 1.) The former two were performed with the annular aluminum entrance exposed to UCN filling the bottle, while the latter two were performed with the stainless steel insert installed at the bottle entrance. As may be seen in Table 1 (see also Fig. 9 in Appendix B), the estimates of N_0 are larger for measurements 13 and 14 than for 16 and 18. This is the case even when the N_0 estimates of measurements 16 and 18 are rescaled to compensate for the decrease in the SUN-2 source output (see the discussion in Sect. 4.4), which was about 12% between these sets of measurements. (See also Fig. 10 in Appendix B for plots of the source output and reactor power during Cycles 188 and 189.) Although the decrease in N observed at low temperatures discussed in the previous section may play some role in this discrepancy, it is possible that the smaller values of N_0 from measurements 16 and 18 are the result of greater UCN loss during filling. This hypothesis is supported by the simulation results presented in Chapter 4 of Ref. [54], which imply that an increased loss in the guides would not only tend to decrease the initial number of UCN in the storage bottle, but to soften the initial energy distribution of these UCN. We therefore expect that the simulated $n_b(E)$ will be closer to the true energy distribution of UCN for measurements 16 and 18, and use only these data in fitting with Eq. 8 to estimate the η of CYTOP.

In fitting experimental storage data, the value of the reduced chi-squared statistic χ^2_r , obtained using Model 1 (Eq. 3), was used as a benchmark. That is, if the value of χ^2_r returned by a fit using an extended model (Models 2, 3, and 4) was significantly smaller than that of Model 1, then the value of η of the former was also included in calculating

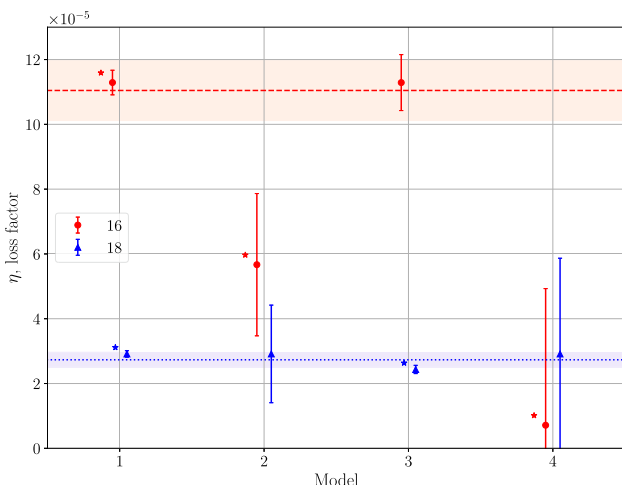


Fig. 8 Plot of the four different model estimates of the η of CYTOP for measurements 16 (red dots) and 18 (blue triangles). (See the text.) The weighted averages of the starred points are shown as the red dashed and blue dotted horizontal lines, with bands indicating uncertainties

a weighted average. Some possible physical explanations for the suitability, or lack thereof, of these models at room temperature and low temperature are considered in Section 5.2 of Ref. [54]. By this method, the weighted average of the results from Models 1, 2, and 4 was taken for measurement 16, giving a final estimate of $\eta = 1.1(1) \times 10^{-4}$ for the loss factor of CYTOP at 295.8 K. For measurement 18, the weighted average of the results from Models 1 and 3 was taken, giving a final estimate of $\eta = 2.7(2) \times 10^{-5}$ at 11.7 K. These low temperature data were corrected before fitting by dividing out the factor $\exp(-t_m/\tau_m)$, as in, for example, Fig. 5a.

Figure 8 shows a graphical representation of the individual model estimates of the loss factor for both measurements 16 and 18. The starred points are those that were used to calculate the final estimates of η , which are shown as banded horizontal lines. As these final estimates are weighted averages, their values are closest to the corresponding points that possess the smallest uncertainties, which happen to be the Model 1 estimates for both measurements. However, unlike the individual estimates of η from measurement 18, those of measurement 16 lie relatively far away from their weighted average, suggesting that—at least at room temperature—the physical picture of the loss mechanism is incomplete. It is thus expected that model-dependent systematic error is the dominant source of uncertainty for the final estimates of the loss factor of CYTOP.

These final estimates are several orders of magnitude larger than the value predicted using only neutron absorption cross sections [56]: $\eta \sim 3 \times 10^{-7}$. However, such disagreement, between measured and predicted loss factors, are commonplace in UCN storage experiments. The measured loss factor of Fomblin grease, for example, is $\eta = 1.8(1) \times 10^{-5}$ at 294 K [44], while its predicted value—due to neutron

absorption—is (also) $\eta \sim 3 \times 10^{-7}$ [23]. Discussions of this “UCN storage anomaly” may be found in several books on UCN physics [26, 57, 58].

6 Conclusion

The fluoropolymer CYTOP shows promise as a coating for UCN storage, especially in cryogenic applications. No evidence of loss of UCN storage performance due to repeated warming and cooling of the bottle was observed. The storage data are well described by a single storage time constant, τ_s , which was found to increase from 311(9) s at room temperature to 564(7) s slightly above 10 K. These values were largely unaffected by a gradual decrease in UCN counts during some measurement series. It is suspected that this effect is associated with residual gases freezing on the cold walls of the experiment at low temperatures.

Estimates of the loss factor of CYTOP were made by combining experimental storage data with simulations of the UCN output of the SUN-2 source. The results are $\eta = 1.1(1) \times 10^{-4}$ at 295.8 K and $\eta = 2.7(2) \times 10^{-5}$ at 11.7 K. It is expected that model-dependent systematic error is the dominant source of uncertainty in these estimates. CYTOP was also found to possess a neutron optical potential of $V = 115.2(2)$ neV, slightly higher than that of Fomblin, $V = 106$ neV [44].

The cryogenic durability of CYTOP and the long storage times achieved in the relatively small bottle used in these studies (3.81) make this new coating material a promising candidate for the production volume of the next generation UCN source SuperSUN, which is currently under construction at the ILL. Measurements using CYTOP coatings for the production volume of the SUN-2 prototype source are the subject of ongoing research.

Acknowledgements The authors gratefully acknowledge support by the Institut Laue-Langevin, and funding from the United States National Science Foundation under Grant No. PHY-2111046.

Data Availability Statement This manuscript has no associated data or the data will not be deposited. [Authors' comment: Data will be provided upon reasonable request.]

Open Access This article is licensed under a Creative Commons Attribution 4.0 International License, which permits use, sharing, adaptation, distribution and reproduction in any medium or format, as long as you give appropriate credit to the original author(s) and the source, provide a link to the Creative Commons licence, and indicate if changes were made. The images or other third party material in this article are included in the article's Creative Commons licence, unless indicated otherwise in a credit line to the material. If material is not included in the article's Creative Commons licence and your intended use is not permitted by statutory regulation or exceeds the permitted use, you will need to obtain permission directly from the copyright holder. To view a copy of this licence, visit <http://creativecommons.org/licenses/by/4.0/>.

Appendix A Neutron reflection and loss

In this appendix, a brief description of neutron reflection and loss at material interfaces is given. The starting point for this discussion is the consideration of a plane wave of energy E in vacuum, incident, at an angle θ to the surface, on an infinite half-space of complex optical potential $U = V - iW$. Defining $E_\perp = E \sin^2 \theta$, the reflection probability may be shown to be the absolute square of the complex quantity

$$R = \frac{\sqrt{E_\perp} - \sqrt{E_\perp - U}}{\sqrt{E_\perp} + \sqrt{E_\perp - U}}, \quad (\text{A1})$$

which is the ratio of the amplitudes of the reflected to the incident wave. This and other expressions may also be represented in terms of either the quantity $k_\perp = k \sin \theta$, where $k = \sqrt{2mE/\hbar^2}$, or—especially in reflectometry—the quantity $Q = 2k_\perp$, the latter of which is commonly referred to as the “wave-vector transfer”.

Confining the present discussion to the UCN energy range, $E < V$, the reflection probability is unity for the case that $W = 0$, that is, $|R|^2 = 1$. When $W > 0$ however, the reflection probability $|R|^2 < 1$, and the quantity $\mu \equiv 1 - |R|^2$ may be interpreted as the loss probability per wall interaction, or per “bounce”. In the limit that $W \ll V$, the loss probability μ may be approximated by its expansion to first order in the loss factor $\eta \equiv W/V$. Assuming also that $W \ll (V - E_\perp)$, this is

$$\mu(E, \theta) = 2\eta \sqrt{\frac{E_\perp}{V - E_\perp}}. \quad (\text{A2})$$

Consider now a storage bottle, which is a closed volume whose walls present the complex potential U to a neutron within its interior. If these walls are not flat on the length scale of UCN wavelengths ($\lambda = h(2m_n E)^{-1/2} \sim 1 \mu\text{m} E^{-1/2}$ for E in units of neV), some degree of non-specular reflection should occur. In this case, it has been argued on the basis of Monte Carlo simulation that, in real bottles, an ensemble of UCN achieves an isotropic velocity distribution within several seconds of storage. (See Section 4.3.2 in Ref. [26].) The angle-averaged loss probability per wall interaction is then [26]

$$\bar{\mu}(E) = 2\eta \left[\frac{V}{E} \arcsin \left(\sqrt{\frac{E}{V}} \right) - \sqrt{\frac{V}{E} - 1} \right], \quad (\text{A3})$$

the magnitude of which is dominated by η . ($\bar{\mu}(E = 0)/\eta = 0$ and $\bar{\mu}(E = V)/\eta = \pi$.) This expression is used in the different models for the loss rate per UCN r discussed in Sect. 5, which are used in Eq. 8 in fitting to experimental storage data.

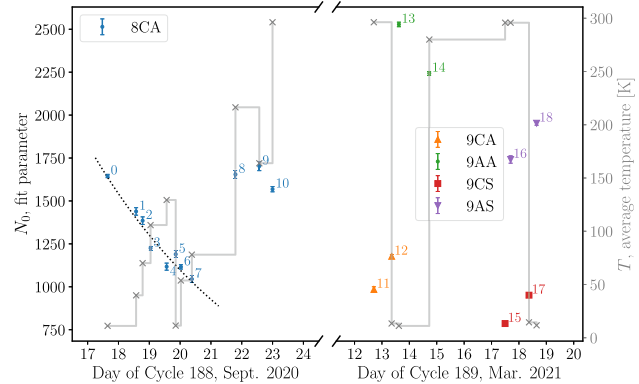


Fig. 9 Gradual decrease over time in the fit parameter N_0 —Eq. 5—during Cycle 188. (Cycle 189 data are included for completeness.) The left vertical axis corresponds to the N_0 values (dots with error bars), while the right vertical axis corresponds to T , the average bottle temperature (gray crosses mark the beginning of a measurement, and horizontal lines show the bottle temperature). Data are labeled by a chronological index given in Table 1, and are also grouped by a three symbol code giving the measurement configuration. (See the caption in Fig. 6.) The black dashed line is a decaying exponential fit to points 0 through 7, which gives a time constant of 120(3) hrs

Appendix B The gradual decrease in N

In addition to the presence of a large vertical spread in some storage curves, as may be seen, for example, in the low temperature data in Fig. 3, evidence of a gradual decrease in N is especially apparent at left in Fig. 9, which shows both the fit parameter N_0 of Eq. 5 (left vertical axis) and the average bottle temperature (right vertical axis), plotted over time during Cycle 188. (Cycle 189 data are included for completeness.) Over the initial four day period of storage measurements performed in Cycle 188 (points labeled 0 through 7, see also Table 1), the bottle temperature was below 130 K, during which time N_0 can be seen to steadily decrease to nearly 50% of its initial value. (As discussed in Sect. 4.4 and as may be seen in Fig. 10, the SUN-2 UCN output varied by less than 3% during Cycle 188, which would seem to exclude the source as a possible cause of the large drop in N_0 .) The bottle was then warmed in order to explore the behavior of τ_s at higher temperature, whereupon it was found that the next storage measurement produced a value of N_0 that had “recovered” to within 10% of its original value.

Similar behavior was observed in measurements at low temperature involving storage bottles with different coatings. (Not reported in this paper.) It is suspected that this effect is associated with residual gases freezing onto the cold walls of the experiment at low temperature. Some degree of gas adsorption is consistent with the observed pressure drop, from roughly 2×10^{-6} mbar to 7×10^{-7} mbar, observed when the system was cooled. (It should be noted that the pressure is measured in the outermost vacuum space of Fig. 2; this region is connected to the guide leading to the storage bottle

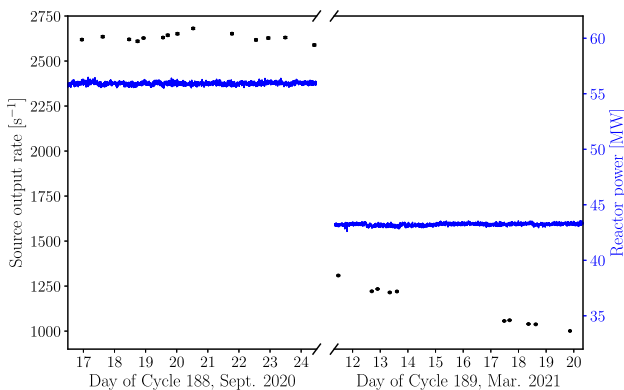


Fig. 10 Source output rate (black points, left vertical axis) and reactor power (blue lines, right vertical axis) during Cycles 188 and 189

only through gaps in the thermal screen followed by a 3 mm hole.)

Appendix C Storage curve model selection

In this appendix, a method of selecting either Eq. 5 or Eq. 7 (containing one additional fit parameter) for use in fitting individual storage data sets is described. The method specifies the amount by which the fit chi-squared statistic χ^2 should decrease in going from Eq. 5 to Eq. 7 before using parameter estimates from the latter. To this end, an “F-test” [59] was used, in which the quantity

$$F = \frac{\chi^2_{v-2} - \chi^2_{v-3}}{\chi^2_{v-3}/(v-3)} \quad (\text{C4})$$

is computed for a data set of size v , where χ^2_{v-2} and χ^2_{v-3} are the weighted sums of the squares of the residuals to fits of Eqs. 5 and 7, respectively. When the improvement in the goodness of fit by the addition of the parameter τ_m in Eq. 7 is appreciable, F will be large. Under the assumption that χ^2_{v-2} and χ^2_{v-3} are chi-squared random variables with $v-2$ and $v-3$ degrees of freedom, respectively, the quantity F should be a random variable described by the F-distribution with 1 “numerator” and $v-3$ “denominator” degrees of freedom [59]. The calculation of F allows for a hypothesis test to be made, in which the null hypothesis is that Eq. 5 is the correct description of a particular data set. In the present work, we reject the null hypothesis—and accept the alternative hypothesis, that Eq. 7 is appropriate—when F is larger than the critical value for the F-distribution which corresponds to a 99% level of confidence.

As an illustration of the method, we provide two examples of the application of this test to data sets from storage measurements 0 and 10, at 10.2 K and 295.0 K, plotted in Fig. 3. (See also Table 1). For measurement 10 with

$v = 38$ points, fits of Eqs. 5 and 7 give $\chi^2_{v-2} = 74.19$ and $\chi^2_{v-3} = 70.93$, respectively, so that $F = (74.19 - 70.93)/[70.93/(38-3)] = 1.60$. The probability that the corresponding random variable, from an F-distribution with 1 numerator and $38-3 = 35$ denominator degrees of freedom, is greater than or equal to this value is approximately 21% (the “p-value”). This is larger than the 1% that would correspond to a 99% level of confidence, and we therefore do not conclude that Eq. 5 provides an insufficient description of these data. In contrast, for measurement 0 with $v = 65$ points, a similar calculation gives $F = 139.1$, which corresponds to a p-value of $2 \times 10^{-15}\%$ for an F-distribution with 1 numerator and $65-3 = 62$ denominator degrees of freedom. We therefore conclude that the use of Eq. 7 in fitting these storage data improves the goodness of fit to a statistically significant level.

References

1. J.M. Pendlebury et al., Phys. Lett. B **136**, 327–330 (1984). [https://doi.org/10.1016/0370-2693\(84\)92013-6](https://doi.org/10.1016/0370-2693(84)92013-6)
2. P.G. Harris et al., Phys. Rev. Lett. **82**, 904–907 (1999). <https://doi.org/10.1103/PhysRevLett.82.904>
3. C.A. Baker et al., Phys. Rev. Lett. **97**, 131–801 (2006). <https://doi.org/10.1103/PhysRevLett.97.131801>
4. J. Pendlebury et al., Phys. Rev. D **92**, 092–003 (2015). <https://doi.org/10.1103/PhysRevD.92.092003>
5. C. Abel et al., Phys. Rev. Lett. **124**, 81–803 (2020). <https://doi.org/10.1103/PhysRevLett.124.081803>
6. W. Mampe, P. Ageron, C. Bates, J.M. Pendlebury, A. Steyerl, Phys. Rev. Lett. **63**, 593–596 (1989). <https://doi.org/10.1103/PhysRevLett.63.593>
7. A. Serebров et al., Phys. Lett. B **605**, 72–78 (2005). <https://doi.org/10.1016/j.physletb.2004.11.013>
8. A. Pichlmaier, V. Varlamov, K. Schreckenbach, P. Geltenbort, Phys. Lett. B **693**, 221–226 (2010). <https://doi.org/10.1016/j.physletb.2010.08.032>
9. A.P. Serebrov et al., Phys. Rev. C **97**, 055–503 (2018). <https://doi.org/10.1103/PhysRevC.97.055503>
10. B. Plaster, et al., EPJ Web Conf. **219**, 04,004 (2019). <https://doi.org/10.1051/epjconf/201921904004>
11. R. Golub, J.M. Pendlebury, Phys. Lett. A **53**, 133–135 (1975). [https://doi.org/10.1016/0375-9601\(75\)90500-9](https://doi.org/10.1016/0375-9601(75)90500-9)
12. R. Golub, J.M. Pendlebury, Phys. Lett. A **62**, 337–339 (1977). [https://doi.org/10.1016/0375-9601\(77\)90434-0](https://doi.org/10.1016/0375-9601(77)90434-0)
13. E. Korobkina, R. Golub, B. Wehring, A. Young, Phys. Lett. A **301**, 462–469 (2002). [https://doi.org/10.1016/S0375-9601\(02\)01052-6](https://doi.org/10.1016/S0375-9601(02)01052-6)
14. K.K.H. Leung, et al., EPJ Web Conf. **219**, 02,005 (2019). <https://doi.org/10.1051/epjconf/201921902005>
15. D. Wurm, et al., EPJ Web Conf. **219**, 02,006 (2019). <https://doi.org/10.1051/epjconf/201921902006>
16. O. Zimmer, R. Golub, Phys. Rev. C **92**, 015,501 (2015). <https://doi.org/10.1103/PhysRevC.92.015501>
17. P. Schmidt-Wellenburg et al., Nucl. Instrum. Methods Phys. Res. A **611**, 267–271 (2009). <https://doi.org/10.1016/j.nima.2009.07.096>
18. O. Zimmer, P. Schmidt-Wellenburg, M. Fertl, H.F. Wirth, M. Assmann, J. Klenke, B. van den Brandt, Eur. Phys. J. C **67**, 589–599 (2010). <https://doi.org/10.1140/epjc/s10052-010-1327-1>

19. F.M. Piegsa, M. Fertl, S.N. Ivanov, M. Kreuz, K.K.H. Leung, P. Schmidt-Wellenburg, T. Soldner, O. Zimmer, Phys. Rev. C **90**, 015,501 (2014). <https://doi.org/10.1103/PhysRevC.90.015501>
20. K.K.H. Leung, Ph.D. thesis, Technische Universität München (2013)
21. K.K.H. Leung, S. Ivanov, F.M. Piegsa, M. Simson, O. Zimmer, Phys. Rev. C **93**, 1–12 (2016). <https://doi.org/10.1103/PhysRevC.93.025501>
22. L. Babin, Ph.D. thesis, Université Grenoble Alpes (2019)
23. Y.N. Pokotilovski, Nucl. Instrum. Methods Phys. Res. A **554**, 356–362 (2005). <https://doi.org/10.1016/j.nima.2005.07.026>
24. W.A. Lanford, R. Golub, Phys. Rev. Lett. **39**, 1509–1512 (1977). <https://doi.org/10.1103/PhysRevLett.39.1509>
25. M.G.D. Van Der Grinten, J.M. Pendlebury, D. Shiers, C.A. Baker, K. Green, P.G. Harris, P.S. Iaydjiev, S.N. Ivanov, P. Geltenbort, Nucl. Instrum. Methods Phys. Res. A **423**, 421–427 (1999). [https://doi.org/10.1016/S0168-9002\(98\)01338-2](https://doi.org/10.1016/S0168-9002(98)01338-2)
26. R. Golub, D.J. Richardson, S.K. Lamoreaux, (CRC Press, New York, 1991). <https://doi.org/10.1201/9780203734803>
27. A. Steyerl, H. Vonach, Z. Phys. A **250**, 166–178 (1972). <https://doi.org/10.1007/BF01386947>
28. L.I. Schiff, Quantum Mechanics (McGraw-Hill, New York, 1968)
29. P.A. Zyla et al., Prog. Theor. Exp. Phys. **2020**, 1–2093 (2020). <https://doi.org/10.1093/ptep/ptaa104>
30. S.J. Seestrom, et al., Phys. Rev. C **92**, 065,501 (2015). <https://doi.org/10.1103/PhysRevC.92.065501>
31. S.J. Seestrom, et al., Phys. Rev. C **95**, 015,501 (2017). <https://doi.org/10.1103/PhysRevC.95.015501>
32. V.K. Ignatovich, Phys. Status Solid B **71**, 477–486 (1975). <https://doi.org/10.1002/pssb.2220710208>
33. S. Degenkolb, P. Nordin, T. Saerbeck, Measurements of SLD and sample characterization for thin films (2021). <https://doi.org/10.5291/ILL-DATA.TEST-3178>
34. T. Saerbeck, R. Cubitt, A. Wildes, G. Manzin, K.H. Andersen, P. Gutfreund, J. Appl. Crystallogr. **51**, 249–256 (2018). <https://doi.org/10.1107/S160057671800239X>
35. C.J. Brinker, in Chemical Solution Deposition of Functional Oxide Thin Films, ed. by T. Schneller, R. Waser, M. Kosec, D. Payne (Springer-Verlag, Wien, 2013), pp. 233–261. https://doi.org/10.1007/978-3-211-99311-8_10
36. A. G. C. Chemicals Inc. Amorphous Fluoropolymer CYTOP (2018). https://www.agc-chemicals.com/file.jsp?id=jp/en/fluorine/products/cytop/download/pdf/CYTOP_EN_Brochure.pdf
37. P. Gutfreund, T. Saerbeck, M. Gonzalez, E. Pellegrini, M. Laver, C. Dewhurst, R. Cubitt, J. Appl. Crystallogr. **51**, 606–615 (2018). <https://doi.org/10.1107/S160057671800448X>
38. A.R.J. Nelson, C.D. Dewhurst, J. Appl. Crystallogr. **47**, 1162–1162 (2014). <https://doi.org/10.1107/S1600576714009595>
39. A. Nelson, J. Appl. Crystallogr. **39**, 273–276 (2006). <https://doi.org/10.1107/S0021889806005073>
40. R.J. Archer, J. Electrochem. Soc. **104**, 619 (1957). <https://doi.org/10.1149/1.2428428>
41. R. Pynn, Phys. Rev. B **45**, 602–612 (1992). <https://doi.org/10.1103/PhysRevB.45.602>
42. J.A. Nelder, R. Mead, Comput. J. **7**, 308–313 (1965). <https://doi.org/10.1093/comjnl/7.4.308>
43. M. Hainbuchner, E. Jericha, Neutron Scattering Lengths (2001). <http://www.ati.ac.at/~neutrop/scattering/ScatteringLengthsAdvTable.pdf>
44. D.J. Richardson, J.M. Pendlebury, P. Iaydjiev, W. Mampe, K. Green, A.I. Kilvington, Nucl. Instrum. Methods Phys. Res. A **308**, 568–573 (1991). [https://doi.org/10.1016/0168-9002\(91\)90069-3](https://doi.org/10.1016/0168-9002(91)90069-3)
45. D. Ruhstorfer, Bachelor's thesis, Technische Universität München (2014)
46. T. Brenner, et al., Appl. Phys. Lett. **107**, 121,604 (2015). <https://doi.org/10.1063/1.4931388>
47. D. Windmayer, Master's thesis, Technische Universität München (2014)
48. J. Hingerl, Master's thesis, Technische Universität München (2019)
49. M. Kuzniak, Ph.D. thesis, Jagiellonian University (2008)
50. K. Bodek et al., Nucl. Instrum. Methods Phys. Res. A **597**, 222–226 (2008). <https://doi.org/10.1016/j.nima.2008.09.018>
51. V. Bondar, et al., Phys. Rev. C **96**, 035,205 (2017). <https://doi.org/10.1103/PhysRevC.96.035205>
52. L.V. Groshev, V.N. Dvoretskij, A.M. Demidov, S.A. Nikolaev, V.I. Lushchikov, Y.N. Panin, Y.N. Pokotilovskij, A.V. Strelkov, F.L. Shapiro, JINR Dubna Commun. (P3-7282) (1973)
53. A. Saunders, et al., Rev. Sci. Instrum. **84**, 013,304 (2013). <https://doi.org/10.1063/1.4770063>
54. T. Neulinger, Ph.D. thesis, University of Illinois Urbana-Champaign (2021). <http://hdl.handle.net/2142/113812>
55. A.G. Frodesen, Probability and Statistics in Particle Physics (Universitetsforlaget, 1979)
56. V.F. Sears, Neutron News **3**, 26–37 (1992). <https://doi.org/10.1080/10448639208218770>
57. V.K. Ignatovich, *The Physics of Ultracold Neutrons* (Clarendon Press, Oxford, 1990)
58. A. Steyerl, Ultracold Neutrons (World Scientific, Singapore, 2020). <https://doi.org/10.1142/11621>
59. P.R. Bevington, Data Reduction and Error Analysis for the Physical Sciences, 2nd edn. (McGraw-Hill, New York, 1992)